RSC Applied Interfaces

ROYAL SOCIETY OF CHEMISTRY

PAPER

View Article Online
View Journal

Cite this: DOI: 10.1039/d5lf00350d

Interfacial synergy between biogenic silica and reduced graphene oxide: experimental and theoretical insights into cationic pollutant adsorption

Mayara Bitencourt Leão,[a] Mônica Carla Lopes,[b] Laura F. O. Vendrame,[c] Leonardo Costa Dias,[a] Ivana Zanella,[c] Solange B. Fagan,[c] Robert Burrow,[b] Iuri Medeiros Jauris[d] and Carolina Ferreira de Matos Jauris *[ab]

Understanding how carbon–silica interfaces govern molecular adsorption remains a key challenge in the design of sustainable hybrid nanomaterials. In this work, a biogenic silica (RHA)/reduced graphene oxide (rGO) hybrid material was synthesized through an aqueous reduction route that promotes direct Si–O–C coupling between rice husk ash and graphene layers. The material interface in the nanocomposite exhibits a complex balance of polarity, defect density, and π-conjugation, providing an interesting model system for studying electronic and chemical cooperation in safranin O adsorption. Spectroscopic analyses reveal that the hybridization process induces the formation of Si–O–C bridges and increases the sp^2 defect population, thereby creating highly heterogeneous active sites. Upon safranin O adsorption, FTIR signatures exhibit vibrational shifts consistent with π–π stacking, cation–π interactions, and hydrogen bonding, which are stabilized by interfacial polarization. Surface charge and morphological analyses confirm the coexistence of electrostatic and structural effects. At the same time, DFT calculations reveal strong binding energies (~1.9 eV) and charge redistribution from rGO to the aromatic ring of the dye. Drawing on experimental and theoretical insights, this study elucidates how chemical bonding and electronic coupling at the silica–carbon interface govern the adsorption mechanism at the molecular scale. The RHA–rGO hybrid thus serves as a versatile model for understanding cooperative interactions in complex hybrid surfaces, beyond immediate adsorption metrics.

Received 10th November 2025,
Accepted 13th January 2026

DOI: 10.1039/d5lf00350d

rsc.li/RSCApplInter

Introduction

Circular economy can promote sustainable development by utilizing low-cost materials that enable the use of agro-industrial waste, thereby improving water quality. Among these waste types, rice husk ash (RHA) stands out as a renewable source of amorphous biogenic silica with a highly porous morphology.[1,2] Despite its abundance and environmental relevance, RHA itself presents limited efficiency in the adsorption of organic pollutants, due to the low density of active sites and the weak affinity for aromatic molecules.[3]

On the other hand, reduced graphene oxide (rGO) presents a high surface area, an abundance of defects, and π-conjugated domains that interact strongly with aromatic and cationic species.[4] However, rGO suffers from sheet restacking after reduction, which collapses its accessible porosity, reduces adsorption capacity, and increases application costs.[5] In this arrangement, silica can act as an inorganic spacer that prevents the restacking of graphene sheets, as well as provides structural stability and additional adsorption sites.[6] In this sense, a promising strategy consists of hybridizing RHA with rGO, combining the accessibility and low cost of ash with the rich surface chemistry of nanocarbon. Although several studies have already reported RHA-based composites with GO/rGO, most studies emphasize only the adsorption performance, without elucidating the molecular mechanisms responsible for the synergy between the components.[6–8] Recent studies have demonstrated increasing interest in graphene–silica hybrid materials, including systems derived from rice husk ash, for environmental remediation applications. For instance, graphene oxide- and rGO-containing silica materials have been reported for dye and pollutant removal, showing enhanced surface area, structural stability, and adsorption capacity.[9–12]

[a] Environmental Science and Technology Center, Campus Caçapava do Sul, Federal University of Pampa, Caçapava do Sul, Brazil
[b] Chemistry Department, Federal University of Santa Maria, Santa Maria, Brazil. E-mail: carolina.matos@ufsm.br
[c] Physics Department, Franciscan University, Santa Maria, Brazil
[d] School of Sciences, Pontifical Catholic University of Rio Grande do Sul, Porto Alegre, Brazil

More recently, graphene–silica hybrid gels and nanocomposites have also been explored to investigate interfacial effects and adsorption behavior.[13]

In particular, the interplay among electrostatic attraction, textural accessibility (micro- and mesoporosity), and specific interactions, such as π–π, cation–π, and hydrogen bonds, remains poorly understood.[14] The absence of this mechanistic understanding limits the rational design of novel biomass-derived hybrid adsorbents.[10]

In this work, we present a simple *in situ* reduction pathway in which graphene oxide (GO) is chemically reduced in the presence of RHA. The resulting nanocomposite, RHA–rGO, exhibits increased mesoporosity, interconnected channels, and Si–O–C interfacial bonds, which confer stability and better surface accessibility. To better understand the adsorption mechanism, we combined SEM, BET, FTIR, Raman, and surface property (pH_{PZC} and hydrophobicity index) analysis, complemented by computational simulations. This integration allows us to distinguish the electrostatic, structural, and chemical contributions to a sorption process.

The cationic aromatic dye safranin O was used as a molecular model, selected not only for its easy spectroscopic detection, but also because its behavior is similar to that of other important cationic contaminants, such as pesticides and drugs. This approach enables a comprehensive and mechanistic understanding of how the interfacial chemistry of biogenic silica domains is combined with rGO, providing guidelines for the development of sustainable and low-cost hybrid adsorbents.

Experimental

Synthesis of the nanocomposite

The precursor materials for this work, rice husk ash and reduced graphene oxide, were obtained individually. Subsequently, the rice husk ash and reduced graphene oxide nanocomposite were obtained as described below. The rice husk ash used in this work was provided by URBANO Arroz, LTDA, a company located in São Gabriel, RS, Brazil. According to the supplier information, rice husks are burned at 700–800 °C for an estimated time of 6 hours. In this work, rice husk ash will be identified as RHA in both experimental and computational calculations, representing silicon clusters. Reduced graphene oxide (rGO) was obtained from the chemical oxidation of graphite[15] (Sigma Aldrich, <20 μm, synthetic). The resulting graphene oxide (GO) was exfoliated in an ultrasonic bath (1.24 mg mL^{-1}) and then combined with the reducing agent sodium borohydride ($NaBH_4$) at a concentration of 4.0 g L^{-1}. The mixture was refluxed for 3 hours. The rGO was filtered, washed with distilled water, and dried overnight at 60 °C. Finally, to obtain the RHA–rGO nanocomposite, 0.12 g of rice husk ash (RHA), 0.48 g of sodium borohydride ($NaBH_4$), and 120 mL of a graphene oxide (GO) dispersion (1.24 mg mL^{-1}) were refluxed for 3 h, corresponding to a mass ratio of RHA : $NaBH_4$: GO = 1 : 4 : 1.24 (w/w/w). Considering the total GO mass in suspension, this composition corresponds to a $NaBH_4$: GO mass ratio of 4 : 1, ensuring an excess of reducing agent during the *in situ* reduction process. After reflux, the material was washed with deionized water and dried at 60 °C overnight.

Characterization

The morphological characterization of the materials was performed using scanning electron microscopy (SEM) and the Brunauer–Emmett–Teller (BET) method. The morphology of the adsorbent surface was analyzed using a Hitachi TM-3000 scanning electron microscope (Tokyo, Japan). Micrographs were analyzed at magnifications of 200×, 500×, and 1000×. The determination of the surface area and pore size by BET was obtained using Micromeritics ASAP2020N apparatus.

Surface chemical characterization was evaluated by Fourier transform infrared and Raman spectroscopies, pH at the point of zero charge, and hydrophobicity index. Fourier transform infrared spectroscopy data were collected on the dried samples before and after application of the materials, in attenuated total reflectance (ATR) mode using a PerkinElmer Spectrum-Two FTIR spectrometer (PerkinElmer, USA), in the wavenumber range of 400 to 4000 cm^{-1}, with a resolution of 2 cm^{-1}, accumulating 64 scans. The Raman spectra were obtained from the equipment SENTERRA confocal Raman microscope (Bruker), with the laser emitting at 532 nm. The pH at the point of zero charge (pH_{PZC}) for the three materials was defined using a 0.05 mol L^{-1} NaCl solution, with pH adjustments between 2 and 9 using 0.05 mol L^{-1} NaOH or HCl. The material was kept in solution for 48 h, and at the end, the pH variation was calculated from the initial pH × ΔpH graph. The hydrophobicity index (HI) was calculated by the vapor sorption method.[16]

The materials were dried in an oven at 60 °C for 24 hours. Approximately 100 mg of each sample was added to 10 mL beakers inserted into 250 mL reagent bottles containing 40 mL of water or hexane. The bottles were closed and allowed to stand. After 24 h, the beakers were carefully removed from the reagent bottles, and the mass of the materials was determined. The increase in mass during exposure to solvent vapor was used to determine the maximum sorption of water or hexane vapor. The HI was calculated according to the ratio of the mass of hexane sorbed to the mass of water sorbed.

Application as an adsorbent

Kinetic and isothermal studies were performed to determine the adsorption capacity of the three materials for the cationic dye safranin O. The final concentration of safranin O in the solution was quantified using a Kasuaki IL-593 UV-vis spectrophotometer with the aid of UV Professional software at a wavelength of 520 nm. The sorption capacities were determined using eqn (1):

$$q_e = \frac{(C_0 - C_f)}{m} \times V \quad (1)$$

where q_e is the adsorption capacity (mg g^{-1}), C_0 is the initial concentration (mg L^{-1}), C_f is the final concentration (mg L^{-1}), V is the volume (L), and m is the mass (g).

For the kinetic study, 0.0100 ± 0.0008 g of each of the three materials was kept in contact with a 10 mL solution of 10 mg L^{-1} safranin O. The adsorptive capacity of the materials was determined every 30 min during the time necessary to reach equilibrium, and the results were plotted as time × q_t. To construct the adsorption isotherms, 0.0100 ± 0.0008 g of each material was used in 10 mL of safranin O solution with concentrations ranging from 0 to 250 mg L^{-1} for RHA and rGO, and up to 500 mg L^{-1} for RHA–rGO. At the end of 24 h of contact, the safranin O concentration in the solution was determined, and the adsorption capacity was calculated from the $C_e \times q_e$ graphs.

Methodology-*ab initio* simulations

The *ab initio* simulations were carried out using the SIESTA code,[17] based on density functional theory (DFT),[18,19] to investigate the energetic, structural, and electronic properties of (i) safranin O (SF) interacting with a silica cluster (SF + RHA), and (ii) a ternary system composed of rGO, SF, and SRHA (rGO + SF + RHA). The interaction between the structure core and valence electrons was described using Troullier–Martins norm-conserving pseudopotentials. In contrast, the valence wave functions were expanded with a double–ζ basis set including polarization functions (DZP). The exchange–correlation energy was treated within the Generalized Gradient Approximation (GGA) using the Perdew–Burke–Ernzerhof (PBE) functional.[20,21] Because dispersion forces are relevant to π–π and cation–π interactions, absolute binding energies may be underestimated with GGA-PBE; trends are nonetheless consistent across configurations. Although dispersion interactions are not explicitly described at the GGA-PBE level, the relative stability trends and adsorption geometries are expected to be robust. Absolute binding energies should, therefore, be interpreted with caution. Regarding the effect of van der Waals (vdW) corrections, it is well established that schemes such as DFT-D2/D3 or vdW–TS tend to increase the absolute values of adsorption energies, particularly for π–π stacking interactions. Consequently, the inclusion of vdW corrections would likely lead to higher absolute binding energies for the (rGO + SF + RHA) systems. However, previous studies indicate that trends in relative stability, adsorption geometries, and dominant interaction mechanisms (such as hydrogen bonding and π–π interactions) are generally preserved. Thus, this methodological choice allows for a direct comparison with previously published theoretical–experimental studies of graphene oxide systems.[22]

An energy shift of 0.04 eV and a real-space mesh cutoff of 200 Ry were employed. All geometries were fully optimized until the residual forces on each atom were smaller than 0.05 eV $Å^{-1}$.

The binding energy (E_b) was calculated according to eqn (2):

$$E_b = -(E_{A+B} - E_A - E_B) \quad (2)$$

where E_{A+B} is the energy of the interacting systems and E_A and E_B are the isolated energy values.

In this study, the nature of the interactions was assessed based on charge transfer, bond distances, and a comprehensive analysis of the electronic energy levels, following procedures described in earlier studies.[23,24]

Results and discussion

Materials characterization

The study of the material's morphology (structural organization, superficial area, and pore size) was performed using scanning electron microscopy and BET measurements. The macroscopic appearance of the materials after drying further supports these structural differences, as illustrated by the digital photographs provided in the SI (Fig. S1). Fig. 1 shows the scanning electron images of the (a) RHA, (b) rGO, and (c) RHA–rGO samples at different magnifications.

The RHA particles (Fig. 1a1–a3) exhibit a rough and highly porous surface, with irregular clusters and interconnected cavities typical of biomass-derived amorphous silicas.[25] This open morphology favors the diffusion of fluids and ionic species, indicating a structure with high surface accessibility.

The rGO material (Fig. 1b1–b3) exhibits a lamellar, wrinkled texture, characterized by thin sheets that partially restack into compact domains. The abundant ripples and folds are characteristic of reduced graphene oxide and indicate a highly reactive surface, as they expose basal planes and concentrate structural defects. In the RHA–rGO nanocomposite (Fig. 1c1–c3), the rGO sheets surround and coat the RHA particles, forming a continuous and cohesive layer on the silica surface. This arrangement results in spherical agglomerates with a spongy texture and a more compact appearance, suggesting strong interfacial interactions between the carbon sheets and the silanol groups. This arrangement indicates that rGO acts as a conductive coating phase, providing connectivity and structural stability to the composite, while RHA maintains the internal porous texture. Thus, the observed morphology reveals the formation of a hybrid core–shell structure, in which RHA constitutes the inorganic core and rGO serves as a functional coating. This arrangement promotes uniform phase dispersion, enhances surface accessibility, and is likely to lead to a higher adsorption capacity.

The N_2 adsorption/desorption analysis enabled the characterization of the surface texture of materials obtained from rice husk ash (RHA), reduced graphene oxide (rGO), and the RHA–rGO nanocomposite (Table 1).

RHA presented a BET surface area of 95.4 $m^2 g^{-1}$, a total pore volume of 0.098 $cm^3 g^{-1}$, and an average pore diameter of 4.1 nm, indicating a predominantly mesoporous structure with a relevant contribution from micropores. As summarized in Table 1, the micropore volume of RHA is 0.0195 $cm^3 g^{-1}$, which is typical of biomass-derived amorphous silicas, where controlled combustion processes generate interconnected cavities and channels.[26] The type IV adsorption isotherm with H3 hysteresis further confirms the presence of open and non-cylindrical mesopores.[27]

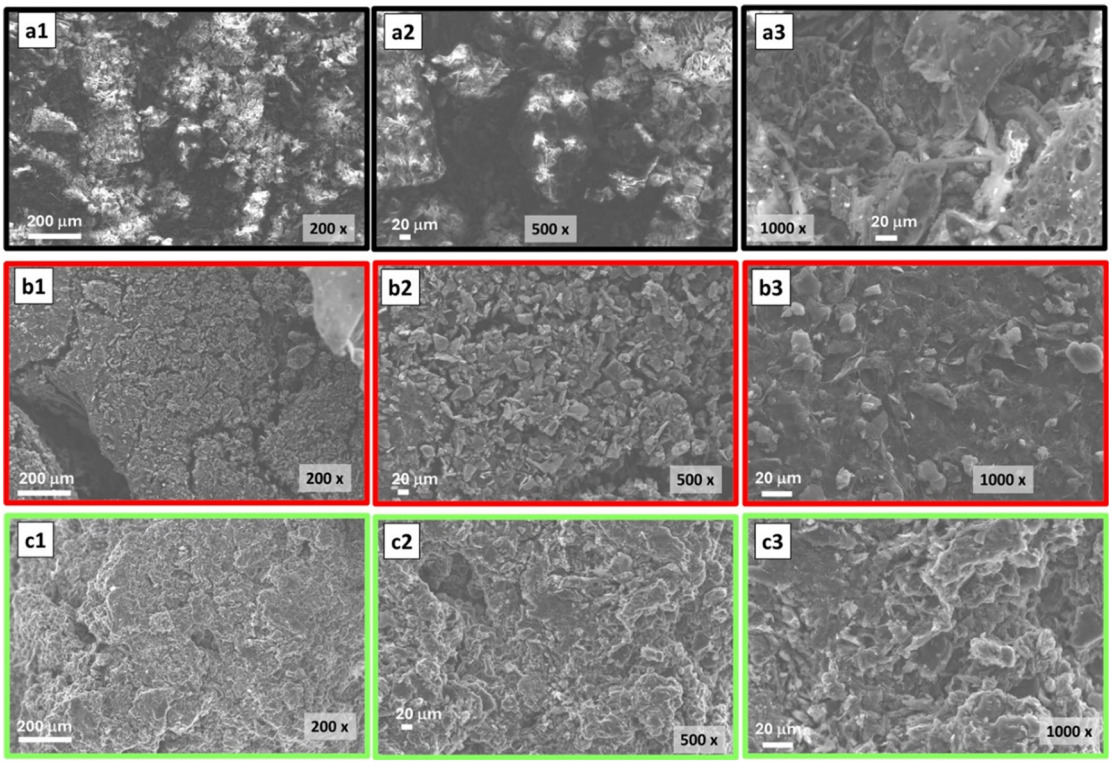

Fig. 1 Scanning electron microscopy images of: (a1–a3) RHA, (b1–b3) rGO, and (c1–c3) RHA–rGO at different magnifications.

Table 1 BET surface area and pore data for RHA, rGO, and RHA–rGO

Sample	Superficial area ($m^2\ g^{-1}$)	Total pore volume ($cm^3\ g^{-1}$)	Average pore diameter (nm)	Micropore area ($m^2\ g^{-1}$)	Micropore volume ($cm^3\ g^{-1}$)
RHA	95.4	0.098	4.1	46.31	0.0195
rGO	91.6	0.031	2.4	69.55	0.0283
RHA–rGO	124.4	0.106	3.4	29.10	0.0124

Reduced graphene oxide (rGO), in turn, exhibits a BET surface area of 91.6 $m^2\ g^{-1}$ and a higher contribution from microporosity, with a micropore volume of 0.0283 $cm^3\ g^{-1}$. This textural feature is consistent with the partial restacking of graphene sheets after chemical reduction and drying, leading to the formation of diffusion-limited micropores and closed nanometric cavities that restrict the access of larger molecules to the internal lamellar domains.

The formation of the RHA–rGO nanocomposite results in a pronounced structural rearrangement. The BET surface area increases to 124.4 $m^2\ g^{-1}$ while the micropore volume decreases significantly to 0.0124 $cm^3\ g^{-1}$. This reduction indicates that some of the micropores become less accessible upon hybrid formation, likely due to partial rGO sheet coating of silica particles and to local pore blocking at the carbon–silica interface. Simultaneously, silica particles act as effective spacers between graphene layers, preventing extensive rGO restacking and promoting the development of a three-dimensional mesoporous network.

The average pore diameter of the nanocomposite (3.4 nm), together with the slight increase in total pore volume (0.106 $cm^3\ g^{-1}$), confirms the formation of a more open and accessible structure dominated by mesopores. This redistribution of porosity from micropores to mesopores increases the external surface area and improves molecular accessibility, which is particularly advantageous for diffusion-controlled adsorption of bulky aromatic molecules such as safranin.

The SEM images corroborate these textural findings. While neat RHA exhibits an irregular and porous morphology and rGO shows partially compacted lamellar sheets, the RHA–rGO nanocomposite displays a rough and continuous surface in which silica domains are distributed between graphene sheets. This physical interaction between the two phases prevents agglomeration, enhances surface roughness, and accounts for the increase in external surface area and mesoporosity, two key parameters governing diffusion and subsequent adsorption.

Similar textural roles of silica acting as a structural spacer to suppress graphene restacking have been reported in recent

graphene–silica hybrid systems, reinforcing the relevance of interfacial organization in controlling surface accessibility and adsorption behavior.[11,13]

Chemical structure

FTIR and Raman spectroscopy analyses were performed to provide an overview of the structural and chemical transformations that occurred during the chemical reduction of graphene oxide over RHA and the subsequent formation of the RHA–rGO nanocomposite.

Fig. 2a shows the FTIR spectra of RHA, GO, rGO, and the RHA–rGO nanocomposite. The RHA spectrum is dominated by characteristic vibrational modes of amorphous silica, including the intense asymmetric Si–O–Si stretching around 1080–1030 cm^{-1}, the symmetric stretching mode near 800 cm^{-1}, and the bending vibration at approximately 460 cm^{-1}, confirming the siliceous network. A weak and broad O–H-related contribution is observed in the 3200–3600 cm^{-1} region, together with a band near 1630 cm^{-1} attributed to the bending vibration of adsorbed water δ(H–O–H). These features are commonly associated with hydrated silanol groups on amorphous silica surfaces and indicate the presence of potential hydrogen-bonding sites. The full FTIR dataset is summarized in Table S1.

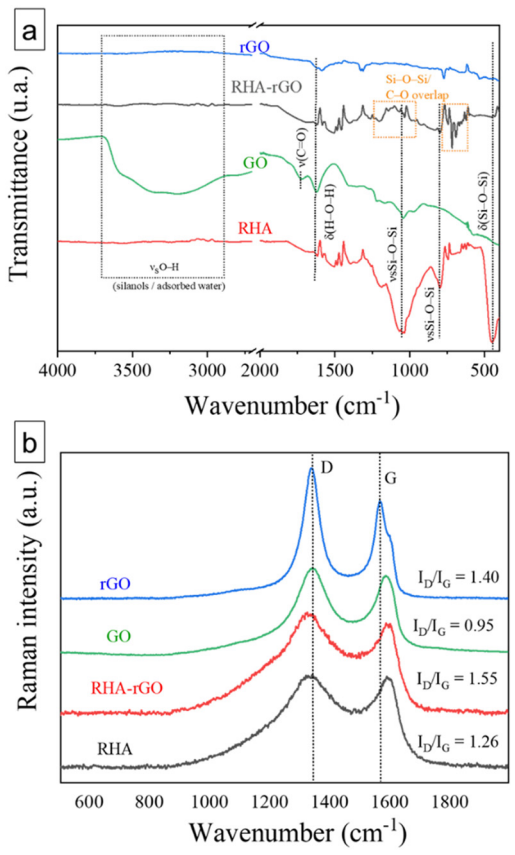

Fig. 2 (a) FTIR-ATR and (b) Raman spectra of RHA, rGO, and RHA–rGO materials.

The GO spectrum shows typical features of highly oxidized graphene sheets, including a broad O–H stretching vibration (3200 to 3500 cm^{-1}), the C═O stretching of carboxylic and carbonyl groups at ~1720 cm^{-1}, C═C stretching from the aromatic backbone near 1610 cm^{-1}, and strong C–O–C/C–O stretching bands (1250–1050 cm^{-1}) associated with epoxide and hydroxyl groups. These bands confirm the presence of extensive oxygen functionalities introduced during the oxidation of graphite.[28] After chemical reduction, the rGO sample shows a marked attenuation of the C═O and C–O stretching bands, consistent with the partial removal of oxygenated groups and the restoration of conjugated sp^2 domains. The residual O–H envelope indicates incomplete reduction, leaving hydroxyls and defect-rich sites that can serve as adsorption centers for organic molecules. Together with the persistence of the aromatic C═C signal, the decrease of oxygenated bands points to the formation of a partially restored π-conjugated network.

In the RHA–rGO nanocomposite, the main siliceous vibration modes remain clearly visible, indicating that the silica framework is preserved. However, subtle spectral changes are observed in the 1100–1000 cm^{-1} region, where the intense Si–O–Si stretching modes of silica overlap with C–O vibrations from the graphene-based phase. The broadening and slight modification of this region, relative to pristine RHA, are consistent with interfacial coupling between the siliceous matrix and rGO. Any contribution from Si–O–C linkages would be expected to occur within this overlapping region and cannot be resolved as an independent vibrational band by FTIR.[29]

Overall, the FTIR results indicate the coexistence of silica and reduced graphene oxide phases in the hybrid material and provide indirect spectroscopic evidence of interfacial interactions, likely involving hydrogen bonding and partial condensation between surface silanol groups and residual oxygenated sites on rGO. Definitive identification of covalent interfacial bonds would require complementary surface-sensitive techniques such as XPS.

While FTIR highlights the chemical evolution of oxygenated and silanol functionalities, Raman provides complementary insights into the electronic and crystallographic organization of sp^2 domains and the extent of disorder introduced by reduction and hybridization. This dual spectroscopic vibrational analysis enables us to correlate chemical functionalization with structural order, explaining the enhanced surface reactivity and adsorption performance of the hybrid toward safranin O.

Fig. 2 presents the Raman spectra of GO, rGO, RHA and RHA–rGO. All spectra display the characteristic D band (1330–1350 cm^{-1}), assigned to the breathing mode of defective sp^2 rings, and G band (1560–1600 cm^{-1}), related to the in-plane C–C stretching of graphitic domains.[30] The full Raman dataset is summarized in Table S2.

The GO spectrum presents the D and G bands at 1341 and 1580 cm^{-1} and an I_D/I_G of 0.95, characteristic of partially oxidized graphitic materials with moderately ordered sp^2 domains. After reduction, rGO exhibits a downshift of the G band to 1567 cm^{-1}, and an increase of I_D/I_G to 1.40, indicating

the creation of new defects and edge sites and, consequently, a higher density of surface-active regions.[31]

The RHA spectrum presents two broad bands at 1337 and 1597 cm^{-1}, with I_D/I_G = 1.26, characteristic of amorphous carbon containing nanometric sp^2 clusters embedded in a siliceous matrix.

In RHA–rGO, D and G bands appear at 1332 and 1569 cm^{-1}, with the highest I_D/I_G (1.55) among all samples. This observation suggests the presence of chemical and electronic interactions between rGO and the RHA matrix, probably mediated by hydrogen bonding and partial Si–O–C linkages between residual oxygenated groups on rGO and silanols on the silica surface. Such interactions modify the electronic environment of rGO, generating local strain and p-type doping, which account for the G-band redshift and the reduction in the structural parameters L_a (from 19.3 to 12.4 nm) and L_D (from 203 to 163 nm).[32]

The increased disorder and the presence of oxygenated functionalities anchored to the silica surface favor both π–π stacking and electrostatic interactions with the cationic safranin O molecules, whose aromatic structure enables strong coupling with the defective sp^2 network. Hence, defect sites and rGO edges act as π-active adsorption centers, while the negatively charged silanol groups of RHA provide additional polar and electrostatic anchoring sites.

The combined FTIR and Raman analyses provide complementary evidence of the structural and chemical integration between rGO and the RHA matrix. FTIR confirms the reduction of GO and reveals spectral features consistent with interfacial coupling between rGO and the silica matrix, while Raman spectroscopy indicates increased disorder and defect density in the carbon framework. It should be noted that FTIR provides indirect evidence of chemical bonding, and XPS analysis would be required for conclusive identification of Si–O–C bonds and surface oxidation states. Together, these results demonstrate that the hybridization process generates a chemically bonded and defect-rich interface, which can enhance surface polarity and electronic heterogeneity, two key features that govern the adsorption of cationic dyes, such as safranin O. Although XPS analysis would further confirm the formation of Si–O–C bonds and clarify the surface oxidation states, the combined FTIR and Raman results, supported by DFT calculations, already provide consistent spectroscopic and electronic evidence of interfacial coupling between rGO and the siliceous matrix.

Finally, pH_{PZC} values (curves in Fig. S2) were 4.3 ± 0.2 (rGO), 4.8 ± 0.2 (RHA–rGO), and 6.9 ± 0.2 (RHA). Thus, at near-neutral pH ($pH > pH_{PZC}$), rGO and the hybrid carry a net negative surface charge, which favors electrostatic adsorption of cationic dyes.[33]

The hydrophobicity indices of the three materials were calculated from the sorption of water or hexane vapor, yielding values of 0.88, 0.82, and 0.85 for RHA, rGO, and RHA–rGO, respectively. A hydrophobicity index less than 1 indicates greater water sorption (polar) than hexane sorption (nonpolar), meaning that the material's surface interacts better with polar solvents. This is due to the presence of oxygenated functional groups, as materials with oxygenated groups on the surface have hydrophilic pores that sorb water vapor. Since the values for all three materials were very close to 1, it can be inferred that all the materials used in this study have a slightly hydrophilic character, which should therefore not significantly affect their adsorptive behavior.[34,35] It is also noted that RHA–rGO presents an intermediate value between RHA and rGO, indicating that the former exhibits an intermediate number of oxygenated groups and hydrophilicity compared to its precursors.

Materials application

Kinetic study

The results for the adsorption kinetics of safranin O dye on RHA, rGO, and RHA–rGO are shown in Fig. 3(a–c) and Table 2. The data were fitted using nonlinear regression with the general-order, pseudo-first-order, and pseudo-second-order kinetic models. From the values of R_{adj}^2 and SD, it is observed that the kinetic model that best fits the data is the general-order one. Despite this, the kinetic equations presented different values for the sorption rate (n), which makes it difficult to compare the kinetic parameters of the models. The observed differences in the n values reflect the distinct structural and chemical characteristics of the materials, as well as the different kinetic pathways involved, and do not limit the applicability of the model.

To better compare the adsorption kinetics, the values of $t_{1/2}$ can be used, which represent the time to obtain half saturation (q_e) in the kinetic results.[36] The $t_{1/2}$ value for safranin O sorption on RHA was 6.9 h, with an equilibrium time of approximately 18 h. For rGO and RHA–rGO, considering the pseudo-second-order model, the $t_{1/2}$ values were 7.6 and 6.9 h, respectively. The equilibrium times for rGO and RHA–rGO were very close, approximately 25 h. These values are higher than those previously found for safranin O sorption ($t_{1/2}$ of 14.4 min and equilibrium in 120 min)[15] and methylene blue ($t_{1/2}$ of 6.59 min and equilibrium in 50 min)[24,37] for a material based on three-dimensional reduced graphene oxide. The main difference between the materials lies in their physical structure, as 3D graphene materials have a more porous structure that should facilitate the adsorption of the investigated analyte.

Furthermore, the drying process of the materials in this study, when compared to the use of hydrogels, is undoubtedly an essential parameter. In this case, the materials in this study have the disadvantage of being oven-dried, which can compact their structure. In the case of rGO, the reduced graphene oxide sheets can be restacked, reducing the specific surface area not only of rGO, but also of RHA–rGO. By verifying that RHA was the material with the shortest adsorption equilibrium time, approximately 8 hours, it is observed that rGO can slow down the adsorption process when aggregated with RHA, thereby requiring the nanocomposite to have a longer contact time with the solution to remove the studied dye.

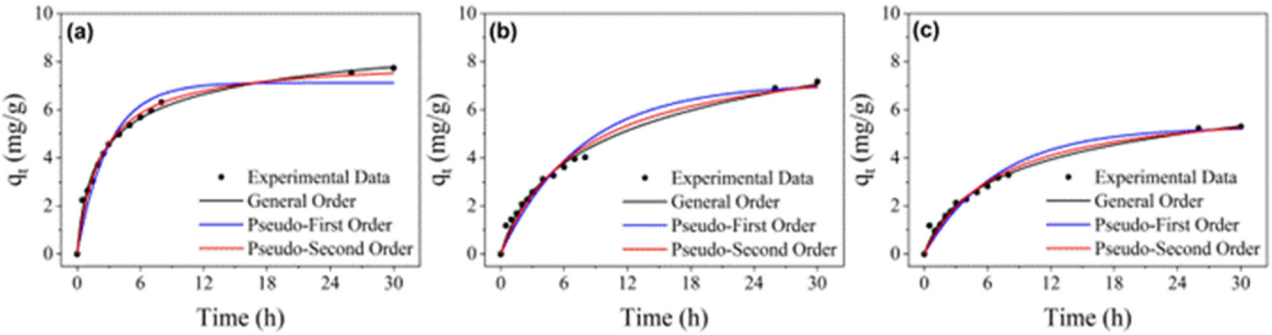

Fig. 3 Kinetic study of adsorption on (a) RHA, (b) rGO, and (c) RHA–rGO. Conditions: adsorbent dosage: 1 g L^{-1}; initial concentration: 10 mg L^{-1}; room temperature.

The shorter $t_{1/2}$ and better pseudo-first order fit for RHA–rGO reflect a higher density of accessible π/Si–OH interfacial sites and stronger electrostatic/π-driven stabilization, in agreement with FTIR/Raman evidence of Si–O–C coupling and, as we will demonstrate in the computational sections, DFT-predicted interfacial polarization.

In summary, the kinetic regime is primarily governed by surface accessibility and site heterogeneity (rate), whereas the ultimate uptake is determined by the equilibrium site population (capacity).

Isotherm equilibrium

The adsorption isotherms for the studied materials are shown in Fig. 4, and the isothermal parameters for each of the nonlinear fits are presented in Table 3. The adsorption isotherms enable the comparison of the performance of different adsorbents for a given adsorbate through the Q_{max} value. Q_{max} is the maximum adsorption capacity of a material, *i.e.*, the amount of adsorbate that an adsorbent can sorb and host, expressed in mg of substance per g of material. The adsorption isotherms were constructed in this work as described in the experimental section, and the experimental results were fitted using the Langmuir, Freundlich, and Sips isothermal models.

From the evaluation of the R_{adj}^2 and SD values for the RHA and rGO materials, a better nonlinear fit was observed using the Freundlich model; for the RHA–rGO material, the Langmuir model presented a better fit to the experimental data. Based on the Langmuir model, the maximum adsorption capacities (Q_{max}) were 143.96 mg g^{-1} for the RHA–rGO nanocomposite, 42.55 mg g^{-1} for RHA, and 41.19 mg g^{-1} for rGO, clearly demonstrating the superior adsorption performance of the hybrid material. These results highlight that although the adsorptive process is slower for RHA–rGO, as observed in the kinetic study, the same material presents greater adsorptive capacities. Therefore, it is observed that RHA–rGO presents a greatly enhanced synergistic behavior, resulting from the combination of RHA and rGO materials. Regarding the best-fitting models, the Freundlich isotherm is an exponential equation that assumes a logarithmic distribution of active sites. The non-saturating behavior observed is consistent with the Freundlich description of heterogeneous surfaces, where q_e grows with C_e within the explored range; this pertains to the equilibrium capacity, not the rate. The Langmuir isotherm predicts monolayer adsorption, with a limited number of sites on the adsorbent surface.[38]

Regarding the adsorption rate, the slightly faster initial uptake observed for RHA compared with rGO and the RHA–rGO nanocomposite can be attributed to its larger average pore diameter and open mesoporous structure, which facilitates the early stage of adsorption dominated by external surface interactions, "flash adsorption".[39] In contrast, rGO contains smaller and partially blocked pores resulting from the restacking of its sheets. At the same time, the composite, despite its higher external surface area, presents a more tortuous pore network at the rGO–silica interfaces.[40] The oxygenated functional groups present in RHA improve the material's wettability and favor the initial adsorption step.[39,40] At the same time, the aromatic rings of safranin O interact strongly with the conjugated carbon domains of rGO through stacking between their planar structures. These combined

Table 2 Kinetics parameters for safranin O adsorption using RHA, rGO, and RHA–rGO

	RHA	rGO	RHA–rGO
General order			
q_e (mg g^{-1})	11.747	43.626	26.70
k_N (g^{n-1} mg^{n-1} min^{-1})	6.58×10^{-5}	3.81×10^{-29}	2.08×10^{-21}
n	4.575	17.441	14.556
$t_{1/2}$ (h)	6.938	—	—
R_{adj}^2	0.991	0.988	0.981
SD	0.202	0.221	0.209
Pseudo-first order			
q_e (mg g^{-1})	7.123	7.072	5.274
K_1 (min^{-1})	0.335	0.132	0.144
$t_{1/2}$ (min)	2.065	5.241	4.836
R_{adj}^2	0.942	0.960	0.958
SD	0.513	0.405	0.312
Pseudo-second order			
q_e (mg g^{-1})	8.094	8.757	6.453
K_2 (g mg^{-1} min^{-1})	0.054	0.015	0.225
$t_{1/2}$ (min)	2.307	7.649	6.878
R_{adj}^2	0.984	0.975	0.973
SD	0.266	0.309	0.250

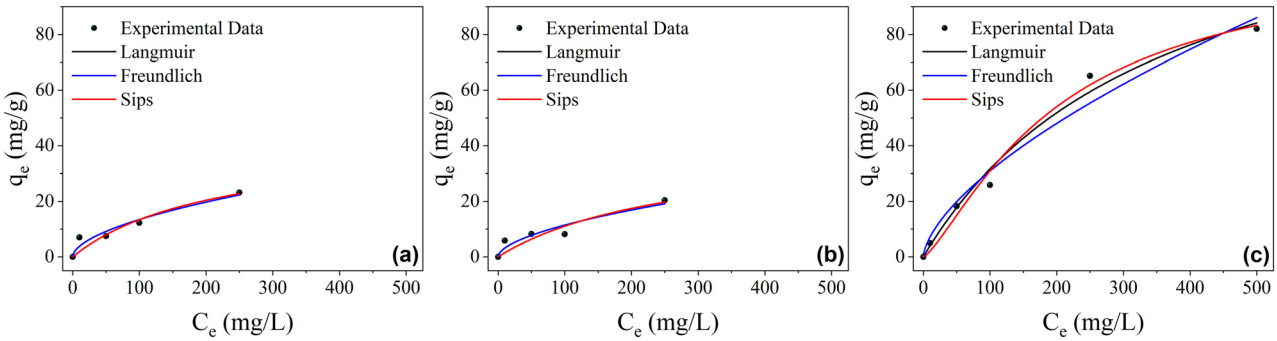

Fig. 4 Adsorption isotherms of (a) RHA, (b) rGO, and (c) RHA–rGO. Conditions: adsorbent dosage: 1 g L^{-1}; initial concentration: 0–500 mg L^{-1}; contact time: 24 hours; room temperature.

Table 3 Isotherm parameters for safranin O adsorption using RHA, rGO, and RHA–rGO

	RHA	rGO	RHA–rGO
Langmuir			
Q_{max} (mg g^{-1})	42.55	41.19	143.96
K_L (L mg^{-1})	0.0046	0.0037	0.0028
R_{adj}^2	0.872	0.807	0.984
SD	3.072	3.266	4.208
Freundlich			
K_F (mg g^{-1})(L $mg^{-1})^{1/n}$	1.052	0.863	1.644
n_F	1.807	1.7819	1.5702
R_{adj}^2	0.929	0.878	0.967
SD	2.283	2.592	6.010
Sips			
Q_{max} (mg g^{-1})	42.548	41.194	108.308
K_S (L mg^{-1})	0.0046	0.0037	9.39×10^{-4}
n_S	1.000	1.000	0.761
R_{adj}^2	0.807	0.711	0.983
SD	3.763	4.001	4.332

effects explain the slower initial rate but higher equilibrium capacity of the composite.

Therefore, the pore size and accessibility play a primary role in the early adsorption kinetics, whereas the surface chemistry and aromatic interactions govern the later stages and overall adsorption performance.

Regarding the influence of surface charge, at near-neutral pH, the sign of the net charge follows the relation pH/pH_{PZC}: surfaces are predominantly negative when pH > pH_{PZC} and positive when pH < pH_{PZC}. Thus, for our materials, rGO exhibits a strong negative charge, the RHA–rGO nanocomposite shows a mildly negative charge, and RHA is close to neutral or slightly positive at a pH of approximately 7. In principle, this favors the electrostatic attraction of a cationic dye such as safranin O in the order rGO ≥ RHA–rGO > RHA.

However, electrostatics governs mainly affinity/initial uptake (*e.g.*, Langmuir/Freundlich constants), while the equilibrium capacity is strongly modulated by textural accessibility and specific interactions. In our case, the RHA–rGO composite combines (i) higher external surface area and accessible mesoporosity (which reduces diffusion limitations) with (ii) aromatic stacking between safranin O rings and conjugated carbon domains from rGO, in addition to polar interactions at silanol/oxygenated sites from RHA. This synergy explains why the composite achieves the highest equilibrium capacity, even though rGO alone is the most negatively charged at neutral pH. The adsorption results are summarized in Table 4 and benchmarked against indexed literature studies.

Adsorption mechanism

Spectroscopic evidence of the adsorption process. The FTIR spectra of rGO, RHA, and RHA–rGO before and after safranin O (Fig. 5) adsorption show some significant spectral modifications that elucidate the adsorption mechanism of the cationic dye on these surfaces.

After adsorption, the spectra of all materials display new or intensified bands within the 1600–1500 cm^{-1} range, attributed to the νC=C and νC=N vibrations of the aromatic phenazinium ring of the dye molecule, confirming successful dye immobilization.

In rGO, more pronounced intensity changes are observed in the aromatic region (1600–1500 cm^{-1}) after adsorption. The emergence and relative intensification of these bands are consistent with π–π stacking interactions between the conjugated sp^2 domains of rGO and the aromatic rings of safranin O. Given the cationic nature of the dye, cation–π interactions with the delocalized π–electron system of rGO may also contribute to adsorption stabilization. In addition, subtle modifications in the broad O–H-related suggest the involvement of residual hydroxyl groups in secondary hydrogen-bonding interactions.[45–47] No new vibrational bands are observed upon adsorption, indicating that the interaction is dominated by non-covalent forces rather than the formation of new chemical bonds.

In the FTIR spectrum of RHA after adsorption of safranin O, the asymmetric stretching mode of Si–O–Si around 1080 cm^{-1} remains clearly visible, with only subtle changes in band shape and relative intensity upon dye adsorption. No new vibrational bands are observed after adsorption, indicating that the interaction between safranin O and the RHA surface does not involve the formation of new chemical

Table 4 Comparison of the performance of materials in removing the safranin O dye from water

Material	Q_{max} (mg g^{-1})	Specific surface area (m^2 g^{-1})	Contact time (h)	Adsorbent dosage (g L^{-1})	Ref.
RHA	49.34	95.35	24	1	This study
rGO	37.03	91.60	24	1	This study
RHA–rGO	148.89	124.28	24	1	This study
3D-rGO	247.8–937.8	62.81–172.27	6	3.2	Leão *et al.*[15]
Castor biomass-based biochar	9.57–17.1	11.51–58.94	4	1	Suleman *et al.*[41]
Silica-based rice husk	18.25	3.47	1	1	Gun *et al.*[42]
Lolium perenne seeds	285.71–322.58	142.32	1	2	Karadeniz *et al.*[43]
Graphene oxide nanoplatelets	487.80	—	2	0.5	Banerjee *et al.*[44]

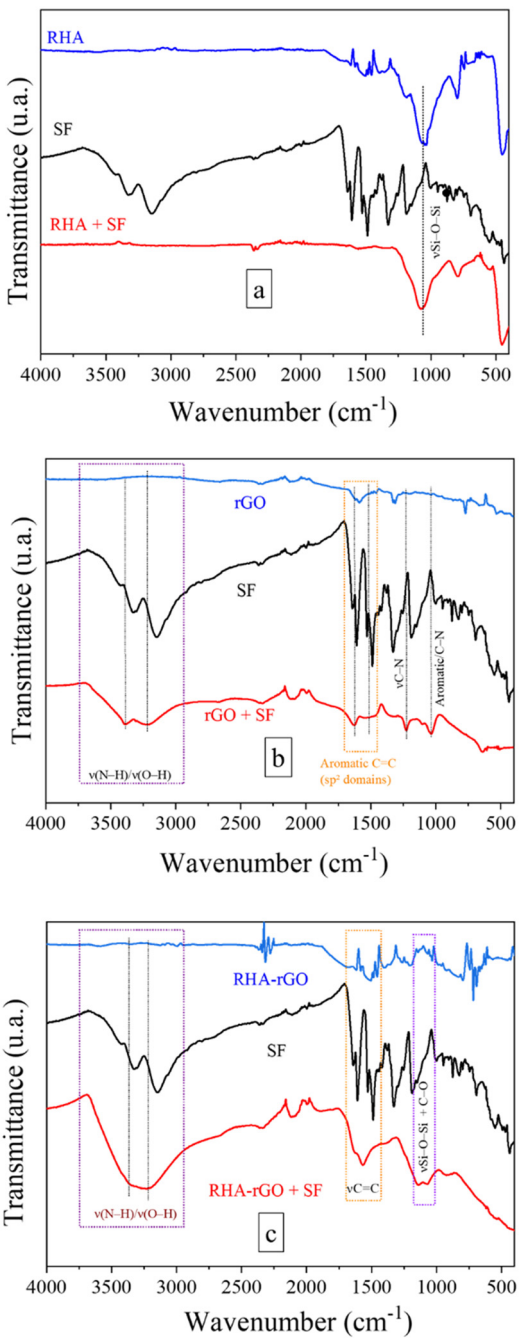

Fig. 5 FTIR spectra of (a) RHA, (b) rGO, and (c) RHA–rGO. Before and after safranin O adsorption.

bonds. These spectral features are consistent with adsorption governed primarily by non-covalent interactions, such as electrostatic attraction between the cationic dye molecules and the negatively charged silanol-rich silica surface.[29]

For the RHA–rGO nanocomposite, the spectroscopic changes observed after safranin O adsorption are markedly more pronounced than those detected for the individual components. A significant intensification and broadening of the ν(N–H)/ν(O–H) in the 3200–3600 cm^{-1} region is observed, together with clear modifications in the fingerprint region. The aromatic νC=C bands in the 1600–1500 cm^{-1} range become more intense, indicating a strong interaction between the aromatic dye molecules and the sp^2 domains of rGO. Simultaneously, noticeable changes in the 1100–1000 cm^{-1} region, where Si–O–Si vibrations of the siliceous matrix overlap with C–O modes from the carbon phase, suggest perturbation of the silica network upon dye adsorption. The combination of these spectral features indicates that adsorption on the RHA–rGO surface involves cooperative interactions between the carbonaceous and siliceous domains, without the formation of new covalent bonds. Overall, the hybrid material provides a heterogeneous interfacial environment that promotes dye stabilization through the combined contributions of π–π interactions within rGO domains and electrostatic and hydrogen-bonding interactions at the silica-rich interface.

These results explain the superior adsorption performance of the RHA–rGO nanocomposite relative to rGO and RHA alone, as the interfacial coupling between the two phases enhances both the density and diversity of adsorption sites.

Computational calculations. To begin with, we examined the electronic features of each isolated component (SF, RHA, and rGO) to identify their most reactive regions. The HOMO–LUMO maps in Fig. S3 (SI) show the orbital distributions and corresponding energy levels. RHA displays a wide energy gap of about 5.6 eV, consistent with values reported for amorphous silica clusters in the literature.[9] SF, in contrast, exhibits an intermediate gap of 1.8 eV, with its frontier orbitals delocalized along the aromatic framework, consistent with previous studies.[48] This pattern suggests that SF can behave as an electron donor or an acceptor, depending on its environment. The rGO system presents the smallest ΔHL (0.58 eV), a value comparable to those from related computational studies employing similar methodologies[49,50] which reflects the high polarizability typical of π-conjugated carbon systems. The

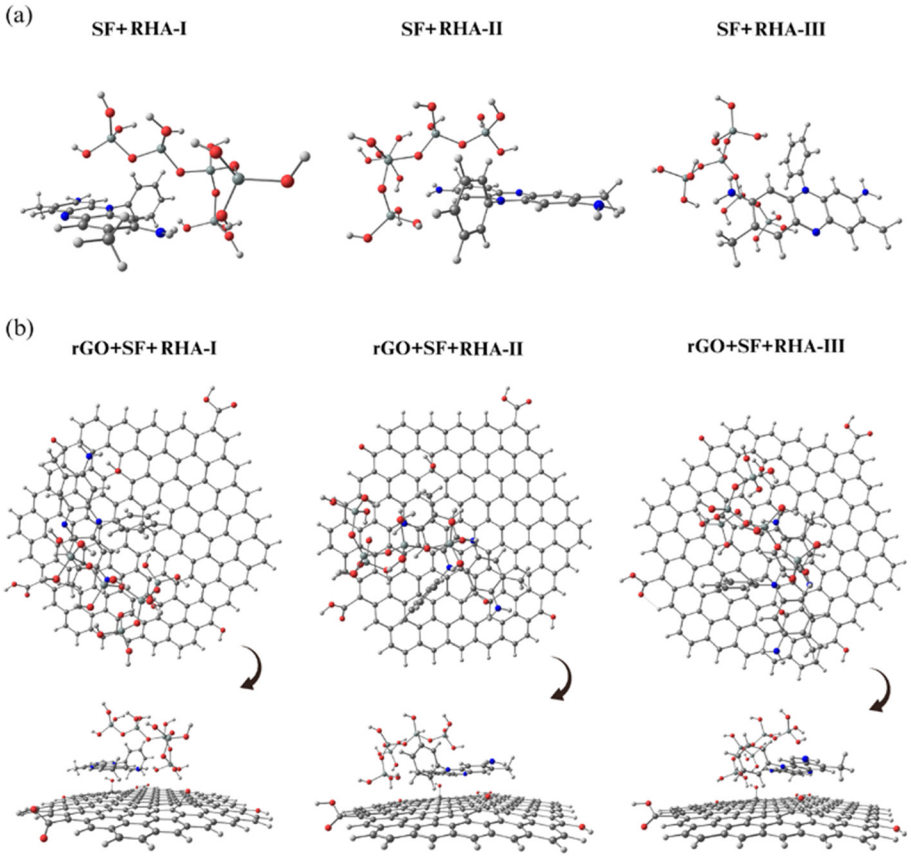

Fig. 6 Most stable optimized geometries of the studied binary systems: (a) SF + RHA (configurations I–III) and the systems: (b) rGO + SF + RHA (configurations I–III).

interaction between the dye molecule and RHA was then explored through different configurations.

As illustrated in Fig. 6a, three stable geometries were obtained for the binary system. The adsorption energies listed in Table 5 range from 0.43 to 0.59 eV, indicating that physisorption is dominated by hydrogen bonding. Among these, the SF + RHA-II configuration (E_b = 0.59 eV) proved to be the most stable. The orbital distribution for this configuration (Fig. S4) shows that the HOMO is localized mainly over the SF molecule, while the LUMO is slightly shared between SF and the silica cluster. The ΔHL value of 1.73 eV suggests a stable complex with moderate electronic coupling. The computed charge-transfer (CT) values (+0.03 to +0.17 e^-) indicate a small electron flow from SF toward RHA, confirming that the silica surface remains nearly neutral. At the same time, the dye makes the most significant contribution to the interaction.

When rGO is introduced, the behavior changes considerably. The ternary rGO + SF + RHA complexes exhibit substantially higher binding energies, ranging from 1.84 to 1.95 eV, with the rGO + SF + RHA-II configuration being the most stable. These values should be interpreted with caution, as dispersion is not explicitly included at the GGA-PBE level. While the relative stability order is robust, the absolute E_b magnitudes are likely underestimated for dispersion-dominated contacts. The ΔHL values decrease sharply to 0.54–0.62 eV, reflecting stronger electronic coupling. The corresponding CT values (−0.03 to +0.18 e^-) indicate that the SF molecule is electronically ambivalent, capable of either donating or accepting electrons, depending on its configuration, consistent with the intermediate HOMO and LUMO positions shown earlier (Fig. S4).

The charge-density maps for rGO + SF + RHA-II (Fig. S5) confirm that the HOMO lies primarily on the rGO surface, while the LUMO is concentrated on SF. This pattern indicates that the interaction involves polarization within the π-system rather than a complete charge transfer. The RHA cluster remains almost neutral, acting mainly as a hydrogen-bonding support that anchors the dye. Although no significant electron delocalization

Table 5 Most stable configurations studied, binding energy (E_b), HOMO/LUMO difference (ΔHL), and charge transfer (CT). Positive values mean electron gain by SF. The most stable configurations are highlighted in bold

Configuration	E_b (eV)	E_b (kcal mol^{-1})	ΔHL (eV)	CT (e^-)
SF + RHA-I	0.44	10.14	1.80	+0.15
SF + RHA-II	**0.59**	**13.60**	**1.73**	**+0.03**
SF + RHA-III	0.43	9.91	1.78	+0.17
rGO + SF + RHA-I	1.88	43.35	0.62	−0.03
rGO + SF + RHA-II	**1.95**	**44.96**	**0.60**	**+0.18**
rGO + SF + RHA-III	1.84	42.43	0.54	+0.12

occurs toward the silica, the inclusion of rGO clearly strengthens the overall binding by enhancing both electrostatic and π–π interactions.

Proposed interaction mechanism. Integrating all experimental and theoretical analyses, a consistent mechanism can be proposed for the adsorption of safranin O onto the RHA–rGO material surface. First, the combination of rGO and RHA creates a chemically and electronically complementary surface: rGO provides a structure rich in defects and π-conjugated domains that are responsible for π–π and cation–π interactions. At the same time, the RHA surface contributes hydroxylated siliceous sites (Si–OH, Si–O$^-$), promoting the hydrogen bonding and electrostatic attraction with the dye. Fig. 7 illustrates the proposed mechanism.

The interfacial coupling through Si–O–C bonds, suggested by FTIR features compatible with Si–O–C formation and supported by DFT calculations, enhances charge heterogeneity and facilitates electron delocalization across the carbon–silica interface.

Raman and SEM data indicate that combining rGO with RHA prevents rGO restacking, thereby generating a hierarchical porous texture with high defect density and accessible adsorption sites. And this is corroborated by the BET results. The negative surface charge (pH > pH_{PZC}) further enhances the attraction of the cationic dye molecules, while computational models reveal strong binding energies and charge transfer from rGO to the safranin O aromatic system.

Our findings demonstrate that the improved performance of the RHA–rGO nanocomposite derives from a multimodal adsorption mechanism that combines electrostatic, π–π, and hydrogen-bonding interactions, amplified by structural and electronic synergy at the carbon/silica interface. This hybridization optimizes both the chemical functionality and textural accessibility of the material, resulting in a highly efficient, sustainable, and robust adsorbent for aromatic cationic dyes.

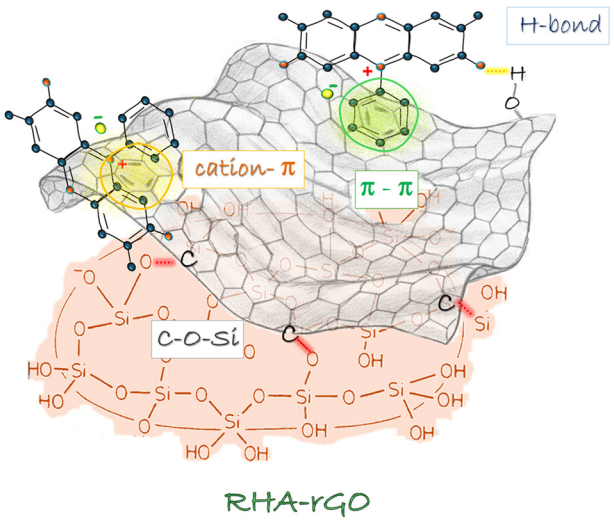

Fig. 7 Schematic illustration of the proposed adsorption mechanism of safranin O on the RHA–rGO hybrid, highlighting π–π stacking and cation–π interactions on rGO domains, hydrogen bonding at silanol sites, and the Si–O–C interfacial region responsible for coupling between the carbon and silica phases.

Conclusion

The combination of biogenic silica and reduced graphene oxide yields a chemically bonded interface, where structural and electronic heterogeneities cooperate to govern molecular adsorption. Integrating all experimental and theoretical analyses, we demonstrate that the RHA–rGO hybrid operates through a multimodal and electronically coupled mechanism, in which π–π and cation–π stacking, hydrogen bonding, and electrostatic attraction occur synergistically at the carbon–silica boundary. The formation of Si–O–C linkages, confirmed by FTIR and supported by DFT, establishes a pathway for charge delocalization between the inorganic and carbonaceous phases. Raman analysis reveals increased disorder and defect-driven π-activity, while BET and SEM reveal a hierarchical micro-mesoporous texture that ensures accessibility to these interfacial domains. The DFT calculations further show that electronic polarization at the rGO–silica interface strengthens noncovalent adsorption energies and stabilizes the dye through charge redistribution.

Together, the results provide a molecular-level understanding of cooperative adsorption at hybrid interfaces, where structural, chemical, and electronic factors converge to govern surface reactivity. This mechanistic insight provides a transferable framework for the rational nanoarchitecture for sustainable carbon–silica materials with tunable interfacial functions. Beyond the specific system studied, this work clarifies how structural, chemical, and electronic heterogeneity governs adsorption at hybrid interfaces, guiding the rational design of multifunctional carbon/silica materials.

Conflicts of interest

There are no conflicts to declare.

Data availability

All data supporting the findings of this study are available within the article. Additional datasets generated and analyzed during the current study are available from the corresponding author upon reasonable request.

Supplementary information (SI) is available. See DOI: https://doi.org/10.1039/d5lf00350d.

Acknowledgements

We thank Prof. Chiara Valsecchi for providing the rice husk ash used in this work, and CENAPAD-SP for the computational time. CFM thanks the financial support from CNPq (405479/2023-9 and 406391/2021-1) and the National Institute of Science and Technology of Carbon Nanomaterials (INCT-Nanocarbon) and

the National Institute of Science and Technology of Nanomaterials for Life (INCT-NanoVida) and FAPERGS (25/2551-0002918-0). During the preparation of this work, the authors used Grammarly to enhance text clarity. The authors critically reviewed, edited, and approved all text and are fully responsible for the content and interpretation presented in this publication.

Notes and references

1 H. K. Okoro, S. M. Alao and S. Pandey, *Appl. Water Sci.*, 2022, **12**, 259, DOI: 10.1007/s13201-022-01778-1.
2 Z. Shamsollahi and A. Partovinia, *J. Environ. Manage.*, 2019, **246**, 314–323, DOI: 10.1016/j.jenvman.2019.05.145.
3 J. Garba, W. A. Samsuri and R. Othman, *Sci. Rep.*, 2019, **9**, 17689, DOI: 10.1038/s41598-019-54079-0.
4 K. Gupta and O. P. Khatri, *J. Colloid Interface Sci.*, 2017, **501**, 11–21, DOI: 10.1016/j.jcis.2017.04.035.
5 R. A. Sukumaran, K. Lakavath, V. V. N. P. Kumar, S. Karingula, K. Mahato and Y. G. Kotagiri, *Nanoscale*, 2025, **17**, 4472–4484, DOI: 10.1039/D4NR04010D.
6 A. Abdelkhalek, M. A. El-Latif, H. Ibrahim, H. Hamad and M. Showman, *Sci. Rep.*, 2022, **12**, 7060, DOI: 10.1038/s41598-022-10602-4.
7 T.-H. Liou and Y.-H. Liou, *Materials*, 2021, **14**, 1214, DOI: 10.3390/ma14051214.
8 M. Handayani, N. Nafi'ah, A. Nugroho, A. Rasyida, A. B. Prasetyo, E. Febriana, E. Sulistiyono and F. Firdiyono, *Crystals*, 2021, **11**, 1337, DOI: 10.3390/cryst11111337.
9 T.-Y. Zhang, Y. Liu, Z. Chen and X. Wang, *Environ. Technol. Innovation*, 2023, **31**, 103270, DOI: 10.1016/j.eti.2023.103270.
10 N. Swetha, V. Anitha, S. Prabhu and M. Rajan, *Mater. Charact.*, 2024, **208**, 114504, DOI: 10.1016/j.matchar.2024.114504.
11 M. Iuliano, S. Esposito, M. Lavorgna and L. Verdolotti, *Surf. Interfaces*, 2024, **43**, 104582, DOI: 10.1016/j.surfin.2024.104582.
12 W. Czepa, D. Pakulski, S. Witomska, V. Patroniak, A. Ciesielski and P. Samorì, *Carbon*, 2020, **158**, 193–201, DOI: 10.1016/j.carbon.2019.11.091.
13 M. González-Barriuso, S. Álvarez-Álvarez, A. Gómez-Rivas and C. Fernández-Blanco, *Gels*, 2025, **11**, 702, DOI: 10.3390/gels11090702.
14 Z. Liu, H. Zeng and M. Qiu, *et al.*, *J. Cleaner Prod.*, 2021, **310**, 127513, DOI: 10.1016/j.jclepro.2021.127513.
15 M. B. Leão, P. C. C. Rosa, C. L. Dalla Corte and C. F. M. Jauris, *Mater. Chem. Phys.*, 2022, **288**, 126408, DOI: 10.1016/j.matchemphys.2022.126408.
16 G. S. dos Reis, M. K. B. Mahbub, M. Wilhelm, E. C. Lima, C. H. Sampaio, C. Saucier and S. L. P. Dias, *Korean J. Chem. Eng.*, 2016, **33**, 3149–3161, DOI: 10.1007/s11814-016-0194-3.
17 J. M. Soler, E. Artacho, J. D. Gale, A. García, J. Junquera, P. Ordejón and D. Sánchez-Portal, *J. Phys.: Condens. Matter*, 2002, **14**, 2745–2779, DOI: 10.1088/0953-8984/14/11/302.
18 W. Kohn and L. J. Sham, *Phys. Rev.*, 1965, **140**, A1133–A1138, DOI: 10.1103/PhysRev.140.A1133.
19 P. Hohenberg and W. Kohn, *Phys. Rev.*, 1964, **136**, B864–B871, DOI: 10.1103/PhysRev.136.B864.
20 J. P. Perdew, K. Burke and M. Ernzerhof, *Phys. Rev. Lett.*, 1996, **77**, 3865–3868, DOI: 10.1103/PhysRevLett.77.3865.
21 O. O. Festus, H. L. Adewumi and I. B. Bamidele, *et al.*, *J. Saudi Chem. Soc.*, 2023, **27**, 101667, DOI: 10.1016/j.jscs.2023.101667.
22 D. Le, A. Kara, E. Schröder, P. Hyldgaard and T. S. Rahman, *J. Phys.:Condens. Matter*, 2012, **24**, 424210, DOI: 10.1088/0953-8984/24/42/424210.
23 C. F. M. Jauris, M. B. Leão, L. F. O. Vendrame and B. L. Mayara, *et al.*, *Front. Carbon*, 2024, **3**, 1305183, DOI: 10.3389/fcarb.2024.1305183.
24 M. B. Leão, L. F. O. Vendrame, S. B. Fagan, I. Zanella, I. M. Jauris, J. R. Bordin and C. F. de Matos, *Mol. Syst. Des. Eng.*, 2023, **8**, 666–678, DOI: 10.1039/D3ME00089A.
25 M. A. Ariff, O. Lin and D.-W. Jung, *et al.*, *Crystals*, 2022, **12**, 1100, DOI: 10.3390/cryst12081100.
26 W. J. Lee, S. L. Bernasek and C. S. Han, *ACS Omega*, 2018, **3**, 11544–11549, DOI: 10.1021/acsomega.8b01453.
27 W. Singhapong, C. Chokethawai, K. Jansuwan, P. Athisakul, P. Palathai, N. Asavavisithchai and P. Jantaratana, *ACS Omega*, 2024, **9**, 5541–5547, DOI: 10.1021/acsomega.3c07569.
28 S. Eigler and A. Hirsch, *Angew. Chem., Int. Ed.*, 2014, **53**, 7720–7738, DOI: 10.1002/anie.201402624.
29 L. Dalstein, E. Potapova and E. Tyrode, *Phys. Chem. Chem. Phys.*, 2017, **19**, 10343–10349, DOI: 10.1039/C7CP01507K.
30 L. M. Malard, M. A. Pimenta, G. Dresselhaus and M. S. Dresselhaus, *Phys. Rep.*, 2009, **473**, 51–87, DOI: 10.1016/j.physrep.2009.02.003.
31 A. Jorio, M. A. Pimenta, A. G. Souza Filho and R. Saito, *Acc. Chem. Res.*, 2015, **48**, 41–47, DOI: 10.1021/ar500280m.
32 L. G. Cançado, A. Jorio and E. H. M. Ferreira, *et al.*, *Nano Lett.*, 2011, **11**, 3190–3196, DOI: 10.1021/nl201432g.
33 M. Kosmulski, *Adv. Colloid Interface Sci.*, 2023, **313**, 102874, DOI: 10.1016/j.cis.2023.102874.
34 W. Huang, W. Li, L. Zhao, Q. Zhang and L. Xu, *Adsorpt. Sci. Technol.*, 2018, **36**, 1691–1703, DOI: 10.1177/0263617417728835.
35 D. Hernández-Monje, L. Giraldo, J. C. Moreno-Piraján and A. M. García, *Molecules*, 2018, **23**, 476, DOI: 10.3390/molecules23020476.
36 P. S. Thue, A. C. Sophia, E. C. Lima, A. G. Wamba, W. S. de Alencar, G. S. dos Reis and S. L. P. Dias, *J. Cleaner Prod.*, 2018, **171**, 30–44, DOI: 10.1016/j.jclepro.2017.10.046.
37 I. M. Jauris, C. F. Matos, C. Saucier, E. C. Lima, A. J. G. Zarbin, S. B. Fagan, F. M. Machado and I. Zanella, *Phys. Chem. Chem. Phys.*, 2016, **18**, 1526–1536, DOI: 10.1039/C5CP05940B.
38 É. C. Lima, M. A. Adebayo and F. M. Machado, in *Carbon Nanomaterials as Adsorbents for Environmental and Biological Applications*, Springer, Cham, 2015, pp. 33–69, DOI: 10.1007/978-3-319-18875-1_2.
39 W. Guo, G. Li, Y. Zheng and K. Li, *RSC Adv.*, 2021, **11**, 34915–34922, DOI: 10.1039/D1RA05255A.
40 T. de F. Neves, N. G. Camparotto, E. A. Rodrigues, V. R. Mastelaro, R. F. Dantas and P. Prediger, *Chem. Eng. J.*, 2022, **431**, 137176, DOI: 10.1016/j.cej.2022.137176.
41 M. Suleman, M. Zafar, A. Ahmed, M. U. Rashid, S. Hussain, A. Razzaq, N. A. Mohidem, T. Fazal, B. Haider and Y.-K. Park, *Sustainability*, 2022, **13**, 6926, DOI: 10.3390/su13126926.

42 M. Gun, H. Arslan, M. Saleh, M. Yalvac and N. Dizge, *Int. J. Environ. Res.*, 2022, **16**(2), 20, DOI: 10.1007/s41742-022-00399-5.
43 S. C. Karadeniz, B. Isik, V. Ugraskan and F. Cakar, *Phys. Chem. Earth*, 2023, **129**, 103338, DOI: 10.1016/j.pce.2022.103338.
44 P. Banerjee, S. Sau, P. Das and A. Mukhopadhayay, *Ecotoxicol. Environ. Saf.*, 2015, **119**, 47–57, DOI: 10.1016/j.ecoenv.2015.04.022.
45 P. R. B. Côrtes, M. B. Leão, G. L. R. Reis, D. D. de Vargas, G. F. Murillo, M. H. Köhler and C. F. de Matos Jauris, *Langmuir*, 2024, **40**, 11173–11183, DOI: 10.1021/acs.langmuir.4c00810.
46 M. B. Leão, A. N. Fernandes and C. F. de Matos Jauris, *ACS Appl. Nano Mater.*, 2024, **7**, 8307–8317, DOI: 10.1021/acsanm.4c01085.
47 W. S. Araújo, C. R. C. Rêgo and D. Guedes-Sobrinho, *et al.*, *ACS Appl. Mater. Interfaces*, 2024, **16**, 31500–31512, DOI: 10.1021/acsami.4c05733.
48 R. Melechalil, K. Arakawa, Y. Hirade, F. Kuttassery, T. Shimada, T. Ishida and S. Takagi, *J. Photochem. Photobiol.*, 2023, **15**, 100182, DOI: 10.1016/j.jpap.2023.100182.
49 V. Oliveira, L. A. Santos, M. N. Baldo and L. Ferreira, *et al.*, *J. Mol. Liq.*, 2020, **321**, 114738, DOI: 10.1016/j.molliq.2020.114738.
50 S. Yadav, N. Goel, V. Kumar, R. Singh and S. Tyagi, *Environ. Sci. Pollut. Res.*, 2018, **25**, 2942–2957, DOI: 10.1007/s11356-017-0596-8.